

# Global three-dimensional simulations of magnetic field evolution in a galactic disk

## II. Gas rich galaxies

S. von Linden<sup>1</sup>, K. Otmianowska-Mazur<sup>2</sup>, H. Lesch<sup>3</sup>, and G. Skupniewicz<sup>2</sup>

<sup>1</sup> Landessternwarte Heidelberg, Königstuhl, D-69117 Heidelberg, Germany

<sup>2</sup> Astronomical Observatory, Jagiellonian University, ul. Orla 171, Kraków, Poland

<sup>3</sup> Universitäts-Sternwarte, Scheinerstr. 1, D-81679 München, Germany

Received; accepted

**Abstract.** A fully three-dimensional computation of induction processes in a disk is performed to investigate the evolution of a large-scale magnetic field in gas-rich barred and spiral galaxies in the presence of field diffusion. As input parameters we use time dependent velocity fields obtained from self-consistent 3D N-body calculations of galactic dynamics. Our present work primarily analyzes the influence of the gas flows in non-axisymmetric gravitational disturbances (like spiral arms and bars) on the behavior of the magnetic field. The magnetic field is found to evolve towards structures resembling dynamical spiral arms and bars, however its distribution is often much more complicated than the velocity field itself. We show that a random configuration of seed magnetic fields quickly dissipates, and is therefore unable to explain the magnetic field strength observed in nearby galaxies. The detailed comparison between the simulated velocity and magnetic fields allows us to establish that the reversals of magnetic vectors appear in the vicinity of the corotation radius of non-axisymmetric disk structures, where the velocity field shows rather abrupt changes. We argue that this explains the observed field reversals in our Galaxy.

**Key words:** MHD – galaxies: magnetic fields – kinematics and dynamics – spiral-galaxies

### 1. Introduction

The origin and evolution of large-scale magnetic fields in galaxies are still not properly understood (e.g. Beck et al. 1996; Lesch & Chiba 1997). There are several issues which are not yet clear. For example, there is still no consensus on the primordial origin of large-scale magnetic fields as proposed by Kulsrud & Anderson (1992). The physical processes initiating and driving turbulent

galactic dynamos may not be able to excite large-scale fields because of the magnetic back reaction on the small scale turbulence (e.g. Cattaneo and Vainshtein 1991). Furthermore, the standard dynamo approach for investigating large-scale magnetic fields does not include the non-axisymmetric part of the galactic velocity field which is able to explain several observed features in barred galaxies (Chiba and Lesch 1994). We concentrate on this second issue in this contribution, which is an extension of our previous work (Otmianowska-Mazur et al. 1997, Paper I). In Paper I, we coupled, for the first time, fully three-dimensional velocity fields resulting from dynamical simulations, with the large-scale magneto-hydro-dynamical evolution. Our main finding was an extremely sensitive response by the magnetic field to spatial variations of the gas velocity field. We concentrated on barred galaxies with normal gas content, where the magnetic vectors are found to show opposite directions along the sides of the bar, and in the course of disk rotation the field vectors are mixed at the ends of the bar. We have also found that the magnetic field lines are well aligned with the bar and the spiral arms.

In the present paper, we generalize our study to consider gas-rich spiral galaxies. The influence of the gas mass and gas contents on the structure and evolution of the magnetic field is discussed.

In the magnetic field simulations, we are interested in galaxies which undergo significant dynamical evolution in terms of bar and spiral arm excitation. It is well known that the intensity of the corresponding dynamical instabilities depends sensitively on the amount of gas in the disk. The higher the gas content the faster and stronger are the excited non-axisymmetric gravitational instabilities which drive the spiral arms (Lynden-Bell & Kalnajs 1972), as can be observed in actual galaxies (Rix & Zaritsky 1995). It is also known that the excitation of such non-axisymmetric structures in disks leads to strong angular momentum transport toward the galactic center (Roberts et al 1979, Toomre 1977, Fuchs & von Linden 1997).

Send offprint requests to: S. von Linden

Correspondence to: svlinden@lsw.uni-heidelberg.de

The angular momentum is either removed from or transferred to the stellar population. This process develops the non-axisymmetric gravitational potential (Schwarz 1981). Since magnetic fields are strongly coupled with gaseous velocity fields, especially the velocity gradient, the amount of gas in the disk will influence the results for the magnetic field evolution as well. In order to study this influence in the present work, we perform calculations with gas masses of 10% and 20% of the total galactic mass. The simulation of a gas-rich galaxy allows us to focus also on proto-galaxies which have not undergone a complete transformation of primordial gas into stars.

## 2. Models and numerical methods

Massive galactic disks are able to form strong elongated bars (Sellwood 1981). This allows us to concentrate on a highly anisotropic velocity distribution accompanied by the development of a bar. Since the growth time scale of a bar increases with the ratio of the halo masses and the disk masses  $M_h/M_d$  (Combes & Sanders 1981) we follow a long-lived strong bar by choosing  $M_{h+b}/M_d = 2$  ( $M_d$ = stellar disk mass,  $M_{h+b}$ = halo and bulge mass). To fulfill the bar instability criterion

$$\Omega_p > (\Omega(r) - \kappa(r)/2), \quad (1)$$

where  $\Omega_p$  is the pattern velocity of the bar,  $\Omega(r)$  is the angular velocity of the disk and  $\kappa(r)$  the epicyclic frequency. The disk has to be massive enough so that the mass in the inner part of the disk reaches a critical mass  $M > M_{crit}$  (Sellwood 1981). We compare our simulations of a gas-rich barred galaxy (model III) with a model presenting only spiral activity in a less massive disk (model IV).

### 2.1. N-body numerical scheme

Our simulations are performed with a 3D N-body code involving a molecular cloud scheme as described by Combes & Gerin (1985) and Gerin et al. (1990). The modeled galaxy is embedded in a spherical halo consisting of visible and dark matter and in a bulge component in the central part of the disk. The galactic disk consists of gas clouds and stellar particles which are interacting via gravity.

The stars interact only by softened gravitational forces, where the softening length  $\epsilon$  is much smaller than the scale height of the disk so that there is practically no artificial stabilization caused by large  $\epsilon$  parameters (Romeo 1994). The gas clouds can interact inelastically, which is simulated in an elaborate cloud-in-cell scheme describing the coalescence and fragmentation of the clouds. We adopt the same scheme and local processes as described by Casoli & Combes (1982) and Combes & Gerin (1985). The clouds encompass masses between  $5 \cdot 10^2$  to  $5 \cdot 10^5 M_\odot$  distributed in 10 mass-bins with logarithmic intervals in order to take into account the power-law variation of the mass spectrum.

Alternative methods to simulate the gas component as a fluid are smoothed particle hydrodynamics (e.g. Friedli & Benz 1993) or finite-difference schemes. Describing the dynamical features in disks, there is no qualitative difference between these codes. In a future work, we will use different schemes for the gas particles to check the influence on the magnetic field.

We perform our simulation with  $N_s \sim 38\,000$  stellar particles. To investigate the influence of the gas particle number on the galactic evolution we perform simulations with  $N_g \leq 38\,000$  and  $\leq 19\,000$ . We use the same grid size and FFT method for the calculation of the gravitational potential as described in Paper I.

The time step  $\delta t$  ( $=10^6$  yr) of the N-body simulation is chosen to fulfill the relation  $v_{phi,max} \delta t \leq l$ , where  $v_{phi,max}$  is the maximum of the rotation curve and  $l$  is the grid length (Combes & Sanders, 1981). The time step for the cloud-cloud collision is about  $10^7$  yr. Several different simulations have been performed, varying the input parameters for the disk, the bulge, the number of gas particles and the gas mass.

### 2.2. Magnetic field evolution model

We analyze the time dependent solutions of the induction equation:

$$\partial \mathbf{B} / \partial t = \text{rot}(\mathbf{v} \times \mathbf{B}) - \text{rot}(\eta \text{rot} \mathbf{B}), \quad (2)$$

where  $\eta$  is the magnetic diffusion coefficient,  $\mathbf{v}$  is the velocity of the gas and  $\mathbf{B}$  is the magnetic field. As in Paper I, the computations are performed with the ZEUS3D code (Stone & Norman, 1992) using only that part which deals with magnetic field evolution. In the original form of the code the constrained transport (CT) algorithm is implemented for the flux-freezing approximation of the eq.(2) ( $\eta = 0$ ). In our analysis, the effects of the magnetic diffusion are introduced in two ways: directly into the code using the CT algorithm and by "pulsed flow" method (Bayly & Childress, 1989) described in Paper I. Both methods fulfill the condition  $\text{div} \mathbf{B} = 0$ .

To incorporate the particle-based velocity field into the grid-based code, a spline function interpolation is applied (cf. Paper I).

The computations have been performed using Cray Y-MP in HLRZ Jülich and Convex Exemplar SPP-1000 Series in ACK CYFRONET-KRAKÓW.

## 3. Input parameters

We study numerically two experiments provided by our 3D particle-mesh scheme simulations: the barred galaxy (case III) and the spiral galaxy (case IV). For both the halo and the bulge components, Plummer spheres are adopted. In all models, the mass and the scale length of the dark matter halo are the same as in Paper I. The model parameters for the N-body calculations are given in Table 1.

Model	III	IV
Mass in $10^{10}M_{\odot}$ :		
- dark-halo mass $M_h$	9.6	9.6
- disk mass $M_d$	7.2	5.8
- gas mass $M_g$	1.6 (0.8)	1.6
- bulge mass $M_b$	4.8	6.2
- mass ratio $(M_d + M_g)/M_{\text{tot}}$	0.38 (0.36)	0.28
Scale length in kpc:		
- dark halo $h$	15	15
- bulge $b$	1.1	1.2
- disk $d$	7	6

**Table 1.** Input parameters for model III and IV

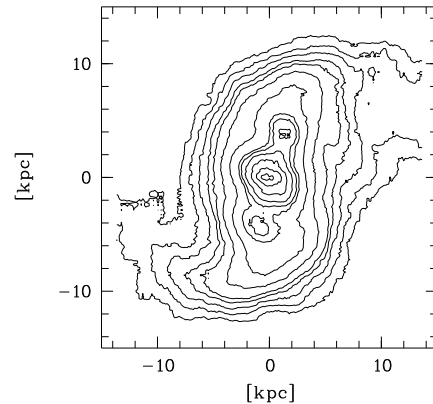
Model	$dx, dy$ [pc]	$dz$ [pc]	$N_x \cdot N_y \cdot N_z$	$\eta$ [cm <sup>2</sup> /s]	Input $B$ -field
IIIa	300	50	101 · 101 · 21	0	toroidal
IIIb	300	50	101 · 101 · 21	$3.2 \cdot 10^{26}$	toroidal
IIIc	300	50	101 · 101 · 21	0	random
IIId	300	50	101 · 101 · 21	$3.2 \cdot 10^{26}$	random
IVa	300	50	101 · 101 · 21	0	toroidal
IVb	300	50	101 · 101 · 21	$3.2 \cdot 10^{26}$	toroidal

**Table 2.** The magnetic field evolution model parameters

**Fig. 1.** Distribution of molecular clouds for the model III projected onto the galactic plane (at  $t = 3.5 \cdot 10^8$  yr.). Massive clouds are plotted with thicker dots as less massive clouds.

The calculations for the magnetic field evolution are performed in 3D rectangular coordinates, where the XY plane is the galactic plane and the Z axis is the axis of galactic rotation. The rectangular size in the X and Y directions is 30 kpc. As a grid interval, we choose the distance of 300 pc resulting in 101 grid points along the X and Y axis. The experiments performed in Paper I have revealed that simulations with twice the distance between the grid points are significantly affected by numerical dissipation due to truncation errors present in the ZEUS3D code (see Paper I, 3.2 and 4.3). Therefore, we decide to adopt a smaller interval which allows us to diminish the numerical diffusion to some extent. The scale height of our model galaxy is 1 kpc with 50 pc as the grid interval (21 grid points along the Z axis). The model input parameters for the magnetic field evolution are summarized in Table 2. The adopted time step of  $10^5$  yr fulfills the Courant condition for the given values of the velocity field and the magnetic diffusion coefficient.

The computations were performed for two initial magnetic field configurations: a purely axisymmetric toroidal field, going in the anti-clockwise direction, and a random field. The strength of the axisymmetric field is  $1 \mu\text{G}$  and

**Fig. 2.** Isophotes of the stellar disk density for the model III (at  $t = 3.5 \cdot 10^8$  yr.).

decreases both toward the galaxy center and toward the edges (see Paper I for a more detailed description). The random field is calculated numerically from a random distribution of the magnetic vector potential  $\mathbf{A}$ . Such a procedure provides us with the magnetic field structure free of magnetic mono-poles. The mean strength of the random field is about  $1 \mu\text{G}$ . As in Paper I, we adopt "out-flow" boundary conditions as the most stable for our calculations. The assumed turbulent diffusion coefficient is  $3.2 \cdot 10^{26} \text{ cm}^2\text{s}^{-1}$  in the XY plane and about  $1.2 \cdot 10^{26} \text{ cm}^2\text{s}^{-1}$  in the Z direction for the experiments IIIb, IIId and IVb (see Table 2). The computations checking the influence of different physical magnetic diffusion values on the magnetic field evolution were made in Paper I. The experiments III and IV last  $6 \cdot 10^8$  yr.

To compare the adopted numerical algorithms for the magnetic diffusion term in the induction equation (2) an initially random field is evolved without any velocity field ( $\mathbf{v} = 0$ ).

#### 4. Pattern velocity and Lindblad resonances

The non-axisymmetric structure in the disk has an angular pattern speed given by the angular velocity  $\Omega_p$ . Three radii in each galaxy are of specific interest because the pattern speed resonates with the eigenfrequencies of the unperturbed galaxy. The first order epicyclic theory (e.g. Binney and Tremaine 1987) superimposes harmonic oscillations on the rotation in both the radial and tangential directions with a characteristic frequency called the epicyclic frequency  $\kappa = 2\Omega \left[1 + \frac{1}{2} \frac{d \ln \Omega}{d \ln r}\right]^{1/2}$ . Thus, in the proper rotating frame, the particle will move in a retrograde sense around a small ellipse, called an epicycle, with axial ratio  $\kappa/2\Omega$ . The resulting motion in the inertial frame is a rosette orbit, generally not closed. To the first approximation, the motion of a gas cloud or a star is thus governed by two frequencies. In a frame corotating with the pattern, the motion is a rosette orbit.

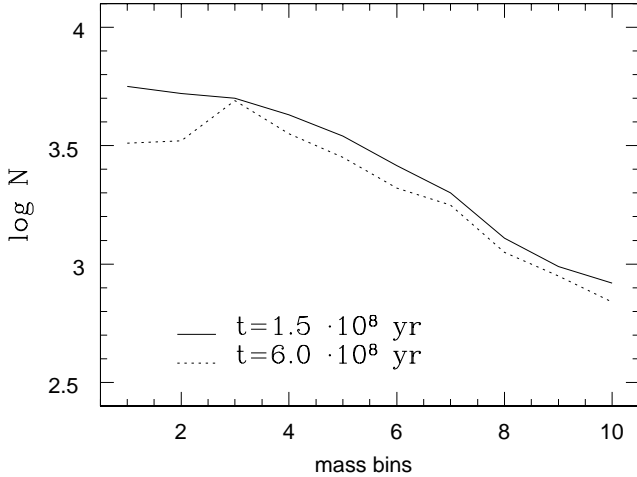


**Fig. 3.** Number density of clouds per mass bin (logarithmic mass intervals) for the model III at  $t = 1.5 \times 10^8$  yr (solid line) and  $t = 6.0 \times 10^8$  yr (dotted line). Mass bin 1 is the lowest cloud mass class ( $5 \cdot 10^2 M_{\odot}$ ); mass bin 10 is the most massive one ( $5 \cdot 10^5 M_{\odot}$ )

tating with a spiral these are  $\Omega(r) - \Omega_p(r)$  and  $\kappa(r)$ . When they are comparable, i.e. when the relative frequency  $\nu = (\omega - m\Omega)/\kappa = m(\Omega - \Omega_p)/\kappa$  is equal to a rational number, we have a resonance. The three main resonances in a galaxy (with a two-arm spiral pattern  $m = 2$ ) are

- the inner Lindblad resonance (ILR) where  $\nu = -1$  and  $\Omega(r) - \kappa(r)/2 = \Omega_p$
- the corotation resonance (CR) where  $\nu = 0$  and  $\Omega(r) = \Omega_p(r)$
- the outer Lindblad resonance (OLR) where  $\nu = +1$  and  $\Omega(r) + \kappa(r)/2 = \Omega_p$

At the Lindblad resonances, the disk and the pattern (bar, spiral arms) intensively exchange energy, mass and angular momentum. The radial velocity, for example, changes its sign at CR. Inside CR, the material flows inward and outside CR it moves outward. Due to the energy and angular momentum transfer, the orbits of the particles change by 90 degrees at every resonance. As we shall see, this simple picture is complicated by the fact that a bar as well as a spiral system has its own resonances. Due to the interaction of the particles with the non-axisymmetric structure, the bar and spiral arms are slowed down, thereby moving the resonance radii outward. Larger portions of the disk are then involved in the radial inflow of the material. Since the resulting disk velocity field, which we use as an input parameter for our magnetic field calculation, reflects this dynamical behaviour, we analyze the pattern velocity and the radii of the Lindblad resonances and corotation in our simulated galaxies.

Based on a Fourier analysis of the density distribution or of the gravitational potential, which allows us to decompose the perturbation present in the galaxy (Junqueira &

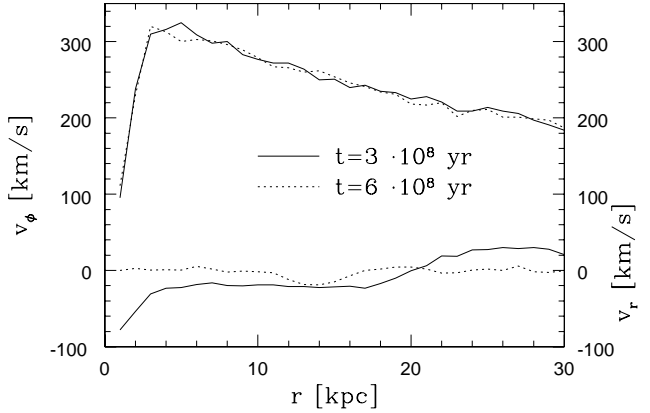


**Fig. 4.** The rotation velocity and the radial velocity at  $t = 1.5 \times 10^8$  yr (solid line) and  $t = 6.0 \times 10^8$  yr (dashed line) for the model III

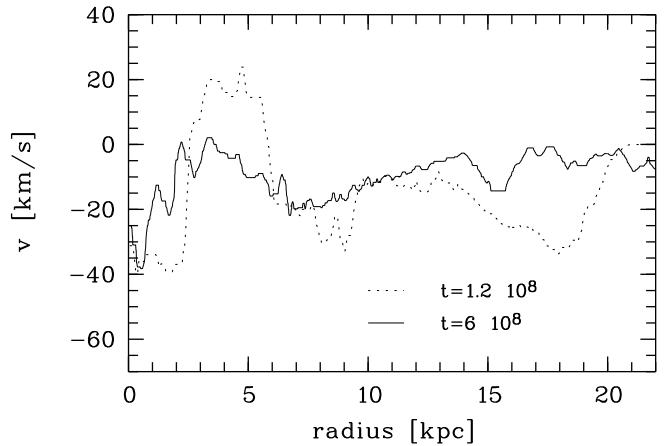


**Fig. 5.** The radial velocity at a 1 kpc thick disk stripe ( $z = 0$ ) at different time step are shown.

Combes 1996), we are able to calculate the pattern velocity of our simulation at different time steps. By plotting the pattern velocity  $\Omega_p$  together with the curves  $\Omega \pm \kappa/2$  we determine the radii of the resonances in the disk.

The uncertainty of the pattern velocity amounts to about  $\pm 2$  km/s/kpc. For the Lindblad radii the error increases from the inner to the outer part of the disk.

## 5. Results of Model III

### 5.1. 3D N-body simulation

Simulations of barred galaxies were performed by several authors (see cf. Katz & Gunn 1991; Gerin et al 1990; Combes & Elmegreen 1993; Norman et al 1996). As in the present calculations, a strong spiral structure is formed first. The two-armed spiral configuration becomes more pronounced and more massive during the next ten time steps. After  $1.5 \cdot 10^8$  yr this structure is clearly visible in the gaseous and stellar disks.

**Fig. 6. a** Magnetic field vectors and the gas density (grey plot) are plotted on the left for the model IIIa at  $t = 1.5 \cdot 10^8$  yr. The belonging intensity of the magnetic field (grey plot) and the radii for the Lindblad resonances for the bar ( $CR_{\text{bar}}$  and  $OLR_{\text{bar}}$ , solid line) and for the spiral system ( $CR_{\text{sp}}$ , dashed line) are shown in the right figure (the  $ILR_{\text{sp}}$  are at the same radius as the  $OLR_{\text{bar}}$ ; the  $OLR_{\text{sp}}$  are located outside the plot range).

**Fig. 6. b** As in Fig. 6a at  $t = 2.5 \cdot 10^8$  yr. The radii of the Lindblad resonances moved outwards during the simulation.

**Fig. 6. c** As in Fig. 6a at  $t = 3.5 \cdot 10^8$  yr. In the inner part of the disk a  $ILR_{\text{bar}}$  appears.

In comparison with model I (see Paper I), experiment III exhibits a higher mass concentration in the central part of the disk due to the assumption of a bulge of smaller scale length. This means that in this model, the bar appears earlier than in case I (after  $2.3 \cdot 10^8$  yr). A second reason for earlier bar formation is the larger amount of gas in the disk (see also Friedli & Benz 1993, Little & Carlberg 1991). After  $2.8 \cdot 10^8$  yr of evolution the bar gets thicker, and during subsequent time-steps the gas concentrates along its major axis. A massive elongated bar is formed which ends near the corotation radius, as in the simulations of Sellwood (1981) and Combes & Sanders (1981).

After  $3.5 \cdot 10^8$  yr the corotation radius of the bar is located at 7.2 kpc. The bar has a length of 14.2 kpc and it concentrates 27% of the disk gas mass (further values are summarized in Tab 3). In the outer part of the disk, a two-armed spiral pattern is still visible (Fig. 1). The pattern velocity and the Lindblad radii are given in Table 3.

The orbits of the bar in the xy plane are similar to those of the 2D-simulation of Sparke & Sellwood (1987) and the 3D simulation of Hasan et al. (1993). The high central gas concentration leads to the appearance of  $x_2$  orbits inside the ILR. Due to the thickness of the bar, these orbits have a large population. We show the isophotes of the stellar disk density in Fig. 2. It is clear that these  $x_2$  orbits create the isophote twist visible in the inner part of the galaxy. The isophote twist is also present in the simulations of Friedly & Martinet (1993) (see e.g. NGC 1422) and it **cannot** be interpreted as a *bar in bar* (Shaw et al. 1993).

The mass spectrum of the molecular clouds changes during the evolution of the disk, which is plotted in Fig. 3 within 30 kpc of the disk. After  $6 \cdot 10^8$  yr there are fewer particles in the disk; in particular the number of low mass clouds decreases because of cloud-cloud collision. The mass spectrum of the clouds in the bar is similar to the mass spectrum of the total disk. However, the percentage of extremely massive clouds in the bar is smaller than that in the disk.

During subsequent evolution, the pattern velocity of the bar slowly decreases and the bar shrinks as in other simulations, cf. Little & Carlberg (1991).

### 5.2. The velocity field

The velocity field of the disk given at different time steps is the input for magnetic field calculation. Fig. 4 presents the rotation curve and the average radial velocity at different time steps calculated in rings of constant distance. Negative  $v_r$  vectors are directed toward the galactic center. Obviously, there is mass transport toward the center, as might be expected. Inside the bar, the radial velocity is dominated by the  $x_2$ -orbit family (Contopoulos & Papayannopoulos 1980) which allows for positive radial velocities. To examine the local radial velocity in more detail, a cut in the disk at  $z = 0$  through the midpoint with a width of 1 kpc is made for two time steps (Fig. 5). At  $6 \cdot 10^8$  yr the cut is taken along the bar. This figure shows that the radial velocity reflects the dynamical behaviour of the disk: e.g. at  $t = 6 \cdot 10^8$  yr the  $ILR_{\text{bar}}$  is located at 3 kpc and  $v_r$  changes sign at this radius.

### 5.3. The 3D evolution of magnetic field: model III

Four simulations of barred gas-rich galaxies have been performed, characterized by the initial configuration of the magnetic field: a toroidal magnetic field with (IIIb) and without magnetic diffusion (IIIa) and a random field with (IIIc) and without diffusion (IIId) (Table 2). In Figs. 6a-d the evolution of the large-scale magnetic field for the case IIIb is presented. We show only the case with non-zero turbulent magnetic diffusion  $\eta$ . However, the computations with  $\eta = 0$  result in similar structures (but with a higher magnetic energy density, see Fig. 8). For the present calculations, the diffusion coefficient  $\eta$  is about three times smaller than in the case Id presented in Paper I, where diffusion significantly influenced the magnetic field behaviour. The models in Paper I are also affected by numerical diffusion. Thus, the present simulations supersede those in Paper I.

At the first evolutionary stage, the magnetic field quickly responds to the velocity shear of the interstellar gas flow in the non-axisymmetric gravitational disturbances. Fig. 6a presents the magnetic field distribution at  $t = 1.5 \cdot 10^8$  yr. The field vectors (left), shown in the galactic plane, are superimposed onto the gas density grey plot (in logarithmic scale). The magnetic field intensity distribution (right) is plotted together with the circles of the

**Fig. 6. d** As in Fig. 6a at  $t = 6.0 \cdot 10^8$  yr. The resonances for the spiral system are outside the plot range.

timestep	$\Omega_{\text{bar}}$	$\Omega_{\text{sp}}$	ILR <sub>bar</sub>	CR <sub>bar</sub>	OLR <sub>bar</sub> = ILR <sub>sp</sub>	CR <sub>sp</sub>	OLR <sub>sp</sub>
[ $10^8$ yr]	[ $\frac{\text{km}}{\text{s kpc}}$ ]	[ $\frac{\text{km}}{\text{s kpc}}$ ]	[kpc]	[kpc]	[kpc]	[kpc]	[kpc]
1.5	66.9	21.9	-	4	6.5	13	18.9
2.5	57.3	14.3	-	5	8.1	18.0	23
3.5	31.8	12.2	2.1	7.2	11.5	24.1	27.3
6.0	25.0	11.0	3	9.9	17.9	29	$\sim 35$
$\pm$	2	2	2.4	2.4	2.6	3	4

**Table 3.** Pattern velocity of the bar and the spiral system (sp) and the radius of the corresponding resonances

Linblad resonances of the the bar (CR<sub>bar</sub> and OLR<sub>bar</sub> solid line) and of the spiral arms (CR<sub>sp</sub> dashed line). From the beginning, the magnetic field closely follows the dynamical spirals resulting in a four-arm pattern visible in the figure. In one of the arms the orientation of the magnetic vectors is opposite to the initial anti-clockwise direction of those in the toroidal magnetic field. This is a result of the strong velocity shears present in this region (see discussion in Sec. 7). There are also two regions with vector reversals located in the inner parts of the next two arms, close to the CR of the bar (see Fig.6a). The magnetic intensity distribution (Fig.6a, right) shows that the magnetic features form nonuniform stripes exhibiting generally spiral structure. Fig.6b presents the magnetic field configuration at  $2.5 \cdot 10^8$  yr. The circles of the resonances for the bar (CR<sub>bar</sub> and OLR<sub>bar</sub>, solid lines) and for the spiral arms (CR<sub>sp</sub>, dashed line) are superimposed onto the intensity grey plot (right). The dynamical structure shows the initial phase of bar formation (see Fig.6b) and two spiral arms. The magnetic field is aligned along the bar and spirals, but its distribution is more complicated. In the central part of the right arm (Fig.6b, left), the magnetic vectors are directed opposite to the vectors at the arm edges (Fig.6b, left), which is also visible in the intensity grey plot (Fig.6b, right). In the upper part of the figure, the region with magnetic vector reversal is still present but the field is weaker than in those magnetic features with an anti-clockwise direction of the vectors (Fig.6b, right). In Fig.6c, we show the magnetic field distribution at  $t = 3.5 \cdot 10^8$  yr. The ILR now appears in the bar. Three resonances (ILR<sub>bar</sub>, CR<sub>bar</sub> and OLR<sub>bar</sub>) for the bar are marked here by solid lines. In the outer part of the disk, the spiral arm system is still visible (see Fig.1). The magnetic field vectors are again aligned with these structures but also form additional arms and regions with vector reversals. As in experiments I and II of Paper I, the magnetic field vectors start to be mixed at both ends of the bar. In Fig.6c, magnetic spiral features form a pattern of four non-uniform spirals (see Fig6c, right). However, there is now a considerable difference between

**Fig. 7.** Topolines of the radial velocity superimposed onto the magnetic intensity grey plot for the simulations IIIb at  $t = 1.5 \cdot 10^8$  yr

the present and  $1.5 \cdot 10^8$  yr time step (Fig.6a). In the previous evolutionary stage, magnetic spiral features closely follow the dynamical spirals. At  $t = 3.5 \cdot 10^8$  yr, the magnetic field has two more arms than the gas (Fig.6c). The regions with vector reversals are still present between the two left magnetic spiral features, along the right side of the bar and in the inner part of the right arm (Fig.6c). A broad bridge of magnetic vectors connects the lower end of the bar with the right side arm and it has no significant dynamical counterpart.

**The main conclusion from these facts is that the magnetic field "remembers" the dynamical disturbances significantly longer than they exist.** At  $t = 6 \cdot 10^8$  yr, the situation is even more evident. The dynamical arms disappear but magnetic spirals remain (Fig.6d). The magnetic field lines are aligned with the bar and create two diffused lanes consisting again of two sub-arms with reversed magnetic vectors (Fig.6d, left). In the right arm, the magnetic intensity is similar to stripes, both, with and without reversal (Fig.6d, right).

The evolution of the galactic magnetic field under the influence of non-axisymmetric gas flows shows that the magnetic field reacts quickly even to weak disturbances in the field. The direction of the magnetic vectors can easily be changed by velocity shear, especially in the regions close to the Lindblad resonances of the bar and in the spiral arms. We could connect these field reversal with the corotation radius of the disk (see discussion in Sec. 7). The numerical simulations also show that magnetic field vectors are mixed at the bar ends, as was shown in Paper I.

In order to analyze the dependence of the magnetic field intensity distribution on the velocity field shear, Fig.7 presents the topolines of the radial velocity  $v_r$  over the magnetic intensity grey plot for the simulations IIIb at

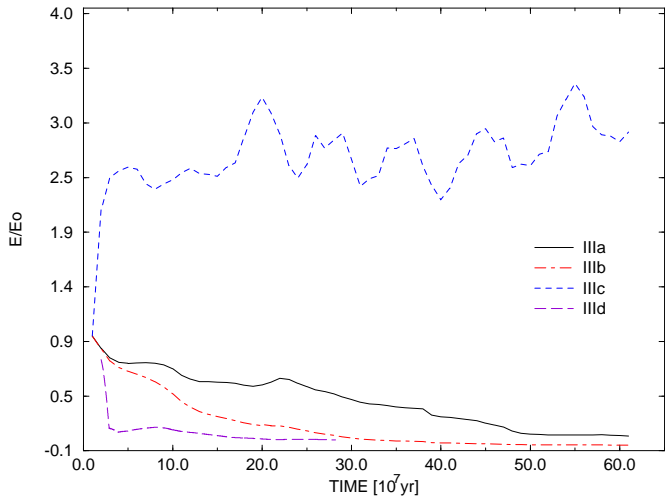


**Fig. 8.** Time evolution of the magnetic energy density  $E$  normalised to the initial energy density  $E_0$  for the models III. The figure legend is in agreement with Table 2

$t = 1.5 \cdot 10^8$  yr. The maximum of the magnetic intensity is located in the region with the strongest gradient of the  $v_r$  component, which coincides with the  $CR_{\text{bar}}$  circle (see Fig.6a). On the inside of the main magnetic spiral features (upper-central part of the figure) the velocity distribution has a maximum, while, on the outside, a minimum is visible (see Fig.7). Both maxima are distributed along the  $OLR_{\text{bar}}$  resonance circle (Fig.6a). The next magnetic arm, which is seen in the lower part of the figure, is also connected with such reversals ( $CR_{\text{sp}}$  radius) of radial velocity. The magnetic strength of this arm is weaker than that of the previous one, but the maxima and minima on both sides of the arm are not so extreme. **This supports the conclusion that the magnetic field reversals appear due to the reversal of the velocity at the CR radii.** The rest of the magnetic features are not so prominent and it is difficult to associate them with changes in the velocity shear.

Fig. 8 presents the time evolution of the magnetic energy density ( $E$ ) normalised to the initial energy density ( $E_0$ ) for the four cases in model III. The parameters of the four cases are given in Table 2. The energy density curves show the time evolution of the toroidal (case IIIa and b) and random (case IIIc and d) input magnetic field structure. Simulation IIIa, with no physical diffusion (solid line), shows a constantly decreasing magnetic energy density due to numerical effects and the lack of strong velocity shears compared to the barred galaxy case in Paper I. However, three small maxima are still present (due to the spiral arms and the bar formation). In model IIIb (dashed-dotted line) the turbulent diffusion diminishes the magnetic energy density much faster than in the previous case. The density for simulation IIIc (short dashed line) with the random input field configuration increases by a factor of 2.5 and then preserves the energy density value

during the whole evolution. This maybe explained by the random character of the initial magnetic field and/or the lack of physical diffusion. The characteristic scale of magnetic field variation has a length of one grid step, so the numerical resistivity is not efficient enough to diminish the field.

The problem of the numerical resistivity was tested in several experiments with different input random field and without physical diffusion. The magnetic energy decreased when the input random magnetic field possessed the scale of change larger than one grid step. The random input magnetic field with magnetic vector randomly distributed at each grid point avoid numerical resistivity. This fact is probably connected with the numerical resistivity which is not strictly a magnetic one (Hawley & Stone, 1995). Stationary fields, for example, do not diffuse away.

All other experiments made with the random magnetic field and with the turbulent diffusion exhibit a rapid decrease in the magnetic energy density which is present in case IIIId (long dashed line). The random magnetic vectors are distributed in all directions and, under the influence of the diffusion, they easily interact, diminishing the magnetic field strength. The decrease of magnetic energy density in each experiment strongly suggests that, in order to explain observed galactic fields, a physical mechanism (e.g. a magnetohydrodynamical dynamo) is necessary for magnetic field amplification on the scale of the whole galaxy.

In order to compare the numerical schemes used in our experiments (the diffusion is implemented directly into the code with the CT algorithm and with the "pulsed-flow" method (see Paper I)), we perform two experiments with random input magnetic field structure and with no velocity field. Both methods give a similar slope of decreasing magnetic energy density. However, the CT scheme maintains a slightly higher magnetic energy density than the "pulsed-flow" method. This is because the "outflow" boundary conditions used in the calculations with the CT method, which are otherwise the most stable for our simulations, exhibit small magnetic monopole values at the boundaries.

## 6. Results of Model IV

### 6.1. 3D N-body simulation for model IV

Model IV also assumes a developing two-armed spiral pattern. This spiral structure transports angular momentum into the outer part of the disk and, outside the corotation radius  $CR_{\text{sp}}$ , the gas particles gain angular momentum. Due to the assumption of a less massive disk in this model, no bar appears in the disk during the simulation. The mass concentration in the inner part of the galaxy is maintained during the evolution, but the arms become weaker and weaker (after approximately  $2.5 \cdot 10^8$  yr). A spiral structure is sharpest at the earliest stages of evolution (see also the simulation in Elmegreen & Tomasson

**Fig. 9. a** Magnetic field vectors and the gas density (grey plot) are plotted left for the model IVb at  $t= 1.0 \cdot 10^8$  yr. The belonging intensity of the magnetic field (grey plot) and the radii for the Lindblad resonances for the spiral system (solid line) are shown in the right figure.

**Fig. 9. b** As in Fig. 9a now for  $t=1.5 \cdot 10^8$  yr. The positions of Lindblad resonances move outward.

timestep	$\Omega_{\text{sp}}$	ILR <sub>sp</sub>	CR <sub>sp</sub>	OLR <sub>sp</sub>
[ $10^8$ yr]	[ $\frac{\text{km}}{\text{s kpc}}$ ]	[kpc]	[kpc]	[kpc]
1.0	28.6.9	2.5	9.0	15
1.5	24.31	3	9.8	17.8
2.0	22.16	3.5	11.3	19.3
2.5	18.59	4.2	13.5	26
$\pm$	2	4	4	4

**Table 4.** Pattern velocity the spiral system and the radius of the resonances for model IV

1993). The vertical scale of the stellar disk changes during evolution from  $\pm 0.5$  kpc ( $1 \cdot 10^8$  yr) to  $\pm 1.5$  kpc ( $2.5 \cdot 10^8$  yr), especially at the outer parts of the disk. The pattern velocity and the resonances of the spiral mode are calculated as described above. At  $1.5 \cdot 10^8$  yr, we find the pattern velocity of the  $m=2$  mode is about 25 km/s/kpc (see Table 4). The spiral structure is visible for the next  $4 \cdot 10^8$  yr.

### 6.2. The 3D evolution of magnetic field: model IV

The evolution of the magnetic field in the spiral galaxy (model IV) is caused by an efficient and fast expulsion of the magnetic field from the central part of the galaxy and is followed for  $4.0 \cdot 10^8$  yr.

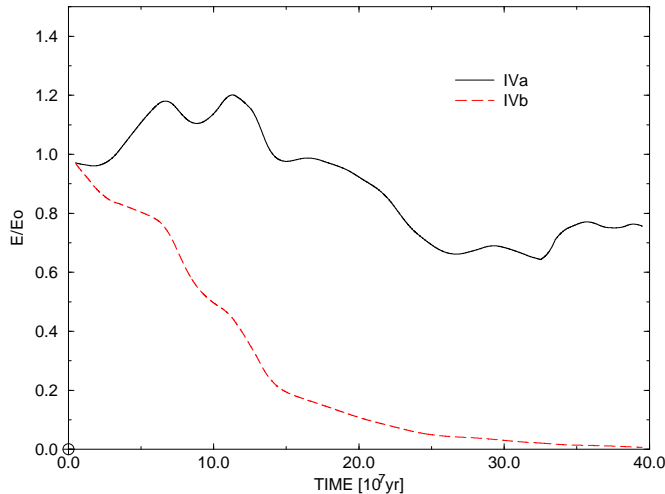
The magnetic field vectors superimposed onto the mass density distribution (grey plot, left) and the magnetic field intensity distribution (grey plot, right) shown together with the Lindblad radii of the  $m=2$  spiral mode system (solid circles) are presented in Fig.9a-c at four times: 1.0, 1.5, 2.0 and  $2.5 \cdot 10^8$  yr for the case IVb.

At  $1 \cdot 10^8$  yr (Fig.9a), the magnetic field forms two diffuse spiral arms. In the arms, the magnetic intensity is non-homogeneous. The areas of stronger and weaker field density are visible, though outside the arms the intensity distribution is more uniform. The field is quickly expelled out of the central part of the galaxy, which possesses a strong mass concentration. This is the case throughout the whole evolution for  $4.0 \cdot 10^8$  yr. At this early stage, the bifurcations of the magnetic spiral features are observed. The magnetic field vectors are aligned along the outer parts of the visible arms and regions of magnetic field reversal become visible (Fig.9a, left). For  $1.5 \cdot 10^8$  yr, the magnetic spiral features become more distinct and characteristic "islands" of stronger fields are visible along

them. Thus, the field is still inhomogeneous and is driven out from the galactic center. It forms a spiral pattern. The magnetic field vectors are aligned along visible arms and reversals are stronger and more clearly visible. Areas with vectors in opposition to the initial toroidal field are again found at the CR circle (see Fig.9a, right). For  $2.0 \cdot 10^8$  yr, the field is driven out of the central part of the galaxy, and the magnetic spiral features are nonuniform. They are clear and sharp at the beginning and more diffused at their ends. They begin to merge with each other so that the reversals almost disappear. The magnetic spirals extend further out of the disk than their dynamical counterparts. The magnetic field intensity starts to develop a ring at the corotation radius. At  $2.5 \cdot 10^8$  yr, the spiral structure of the magnetic arms disappears. The field forms a clear ring outside the dynamical structure, still aligned with the CR circle (see discussion in Sec. 7). Its vectors are in the anticlockwise direction and possess an almost azimuthal component (axisymmetric spiral structure - ASS?). It is still inhomogeneous with "islands" of stronger field density. Very weak magnetic spiral features appear in the center, probably caused by the numerical artifacts.

The magnetic energy density curves for model IV are presented in Fig.10. The experiment with no physical diffusion (IVa, solid line) results in two maxima of magnetic energy density near  $0.7 \cdot 10^8$  yr and  $1.1 \cdot 10^8$  yr. The first maximum is connected with a strong velocity shear due to the initial formation of spiral arms in the galactic disk. The second maximum is the result of the velocity gradient caused by a strong mass transport into the central part of the galaxy. The galaxy develops a massive spiral structure that extends to the centre of the disk. After two maxima, the energy density decreases due to numerical resistivity, but still possesses further maxima caused by continuous changes in the spiral pattern (about  $1.6 \cdot 10^8$  yr) and later at about  $2.9 \cdot 10^8$  yr and  $3.6 \cdot 10^8$  yr. These two maxima are connected with the formation of a small bar in the central part of the galaxy. The magnetic energy density for the case IVb with physical diffusion (dashed line) decreases for the whole evolution showing only small maxima at the same positions as in previous simulations.

The analysis of  $B_z$ , topoline maps made at different heights of the galactic disk, shows that weak magnetic field waving is present in both models (III and IV) (see Paper I for discussion).

**Fig. 9. c** As in Fig. 9a now for  $t=2.0 \cdot 10^8$  yr.**Fig. 9. d** As in Fig. 9a now for  $t=2.5 \cdot 10^8$  yr. The ring for the OLR is now outside the plot range.**Fig. 10.** Time evolution of the magnetic energy density  $E$  normalised to the initial energy density  $E_o$  for the model IV

## 7. Conclusions and discussion

A numerical model involving the three-dimensional and time-dependent velocity of molecular gas is applied to study the evolution of the large-scale magnetic field under the influence of non-axisymmetric dynamical structures. We perform a comparison between bar and spiral arm activity to investigate the effect of the different gas velocity fields. The bar transports much more mass inward and angular momentum outward than the disk with spiral arms alone. Our present work demonstrates that the magnetic field is influenced more strongly by the bar velocity shear than by spiral disturbances. Our main conclusion is:

- The magnetic field dissipates much faster in spiral than in barred galaxies due to the lower level of angular momentum transport.

The number of particles in the gas disk has no significant influence on magnetic field behaviour.

In all experiments, the regions with reversals of the magnetic vectors appear due to velocity shears. We note that:

- Field reversals appear close to the corotation radius

at which, according to standard theory (e.g. Athanassoula 1984), the radial velocity of the gas flow changes its sign. Outside the CR circle, the radial velocity is directed outward while inside the CR, the gas flows inward if the disk has only one resonance system. At the CR, there is a

radial-velocity minimum. Since the magnetic field is coupled to the gradients of the velocity field, it changes its direction as well. In addition to the corotation radius of the bars, there is also a corotation radius of the spiral arms. Similarly, at the  $CR_{sp}$ , the magnetic field changes its direction in response to the varying velocity field at that radius. Such behaviour can be observed in all our simulations but especially in model IV (spiral galaxy) where the obtained ring of magnetic field (Fig.9c & d) shifts together with corotation radius of the spiral arms.

Changes in the velocity field at the inner Lindblad resonance (ILR) are also visible in the magnetic field. The orbits change their sign by 90 degrees at every resonance. Superimposed onto the global galactic rotation, this leads to a large-scale spiral pattern, whose complicated velocity structure is traced by the magnetic field via velocity gradients.

From our numerical experiments, we demonstrate that due to a smaller number of Lindblad resonances in spirals

- the regions of magnetic vector reversals are less significant in spiral than in barred galaxies.

In addition, we have studied how the input magnetic field affects the further development of the magnetic field distribution and its intensity. We have examined purely axisymmetric toroidal fields with an anti-clockwise direction and random seed fields.

The case of non-axisymmetric input magnetic field has been widely discussed in the paper Otmianowska & Chiba (1995). We analyzed the uniform protogalactic magnetic field, distributed along the Y axis. For all experiments, the magnetic field was quickly wound into the bisymmetric structure, causing the initial growth of the magnetic energy. As the time progresses the magnetic field in the inner part of the disk was quickly swept out due to magnetic lines winding mechanism and the magnetic energy always decreased very fast (after  $2 \times 10^8 yr$ ).

In contrast to the computations with a toroidal magnetic field, those with random magnetic fields resulted in an extremely rapid decrease in the magnetic energy density. This suggests, that:

- Random seed magnetic fields in galaxies cannot explain the observed magnetic field in galactic disks.

As an interesting application, we note that observations of the magnetic field in our Galaxy show strong evidence for two reversals of the field vectors (Vallée 1988, 1991, Han & Qiao 1994). Vallée (1997) argues that the region with magnetic vectors directed opposite to the rest magnetic field in our Galaxy (which has a clockwise direction) extends from the Sagittarius arm (about  $r = 6.5$  kpc)

to the location of the Sun ( $7.5 \pm 1$  kpc). **These observed reversals of magnetic field are located in the vicinity of the observed corotation radius in our Galaxy.** Mishurov et al. (1997) estimated the pattern velocity of the spiral pattern as  $\Omega = 28.1 \pm 2.0$ , and this sets the corotation radius of our Milky Way at a radius of  $7.2 \pm 1.3$  kpc. This might confirm the statement that the magnetic field vectors' distribution and direction depend on the dynamical behaviour of the non-axisymmetric structures and the positions of the Lindblad resonances as well. Existing theoretical explanations (e.g. Poezd et al. 1993) concerning the observed reversals in our Galaxy connect them with special conditions of thin dynamo action and with structures inherited from seed magnetic fields. Our results provide a simpler solution to this problem. The regions of magnetic reversal appear due to clear dynamical processes, closely connected with non-axisymmetric features present in a galactic disk. In a future work we will investigate whether there are more such "coincidences" in other galaxies. For example, the ring structure in model IV might be interesting for our neighbouring galaxy M31 in which such a ring was detected 15 years ago by Beck (1982).

However the modeled ring is shifted further from the galactic center than the gaseous arms visible in Fig.9d. The observed magnetic ring coincides with the HI torus at the radius of 10 kpc.

The field reversals are also interesting for comparison with the observations of M81 by Krause et al. (1987a,b), who determined a neutral line at which the magnetic field strength should vanish.

*Acknowledgements.* Part of this work was supported by the Deutsche Forschungsgemeinschaft (Sonderforschungsbereich 328 *Evolution of Galaxies*) SvL thanks Prof. F. Combes for allowing us to use her code and for fruitful discussions. Our thanks to Detlef Elstner for his helpful comments and discussions. KO wishes to express her gratitude to Marek Urbanik & Marian Soida for their valuable advice in the course of this project. Calculations were supported by the Forschungszentrum Jülich GmbH and ACK CYFRONET-KRAKÓW. This work was partly supported by a grant from the Polish Committee for Scientific Research (KBN), grant no. PB/962/P03/97/12. HL thanks Prof. R. Wielebinski and the Deutsche Forschungsgemeinschaft for support (Grant LE 1039/2-1).

## References

Athanassoula E., 1994, Physics Report 114, Nos. 5&6, 319  
 Bayly B., Childress S., 1989, GAFD, 49, 23  
 Beck R., 1982, A&A 106, 121  
 Beck R., Brandenburg A., Moss D. et al., 1996, ARAA 34, 155  
 Binney J., Tremaine S., 1987 "Galactic Dynamics", Princeton University Press, NJ  
 Casoli F., Combes F., 1982, A&A 110, 287  
 Cattaneo, F., Vainshtein, S.I., 1991, ApJ, 376, L21  
 Chiba M., Lesch H., 1994, A&A 284, 731

Contopoulos G., Papayannopoulos T., 1980 A&A 92, 33  
 Combes F., Gérin M., 1985, A&A 150, 327  
 Combes F., Elmegreen B.G., 1993, A&A 271, 391  
 Combes F., Sanders R.H., 1981, A&A 96, 164  
 Elmegreen B.G., Thomasson M., 1993, A&A 272, 37  
 Friedli D., Benz W., 1993, A&A 268, 65  
 Friedli D., Martinet L., 1993, A&A 277, 27  
 Fuchs B., von Linden S., 1998, MNRAS, in press  
 Gerin M., Combes F., Athanassoula E., 1990, A&A 230, 37  
 Han J.L., Qiao G.J., 1994, A&A 288, 759  
 Hasan H., Pfenniger D., Norman C., 1993, ApJ 409, 91  
 Hawley J., Stone J., 1995, Computer Physics Comm. 89, 127  
 Junqueira S., Combes F., 1996, A&A 312, 703  
 Katz N., Gunn, J.E., 1991, ApJ, 377, 365  
 Krause M., Hummel E., Beck R., 1987a, A&A 217,4  
 Krause M., Hummel E., Beck R., 1987b, A&A 217, 17  
 Kulsrud, R.M., Anderson, S.W., 1992, ApJ, 396, 606  
 Lesch H., Chiba M., 1997, Fund. Cosm. Phys. 18, 273  
 Lynden-Bell D., Kalnajs A.J., 1972, MNRAS 157, 1  
 Little B., Carlberg R.G., 1991, MNRAS 250, 161  
 Mishurov Yu.M., Zenina I.A., Dambis A.K., Melnik A.M., Rastorguev A.S., 1997, A&A 323, 775  
 Norman C.A., Sellwood J.A., Hasan H., 1996, ApJ 462, 114  
 Otmianowska-Mazur K., Chiba M., 1995, A&A 301,41  
 Otmianowska-Mazur K., von Linden S., Lesch H., Skupniewicz G., 1997, A&A 323, 560  
 Poezd A., Shukurov, A., Sokoloff, D., 1993, MNRAS, 264, 285  
 Rix H.-W., Zaritsky D., 1995, ApJ 447,82  
 Roberts W.W., Huntley J.M., van Albada G.D., 1979, ApJ 233, 67  
 Romeo A.B., 1994, A&A, 286, 799  
 Schwarz M.P., 1981, ApJ 247, 77  
 Sellwood J.A., 1981, A&A 99, 362  
 Sparke L.S., Sellwood J.A., 1987, MNRAS, 225, 653  
 Stone J.M., Norman M.L., 1992, ApJS 80, 791  
 Shaw M.A., Combes F., Axon D.J., Wright G.S., 1993, A&A 273, 31  
 Toomre A., 1977, Ann. Rev., Astron. Astrophys. 15, 437  
 Vallée J.P., 1988 AJ 95,750  
 Vallée J.P., 1991 ApJ 366,450  
 Vallée J.P., 1997 Fundamentals of Cosmic Physics

This figure "fig1.gif" is available in "gif" format from:

<http://arxiv.org/ps/astro-ph/9801311v1>

This figure "fig6a.gif" is available in "gif" format from:

<http://arxiv.org/ps/astro-ph/9801311v1>

This figure "fig6b.gif" is available in "gif" format from:

<http://arxiv.org/ps/astro-ph/9801311v1>

This figure "fig6c.gif" is available in "gif" format from:

<http://arxiv.org/ps/astro-ph/9801311v1>

This figure "fig6d.gif" is available in "gif" format from:

<http://arxiv.org/ps/astro-ph/9801311v1>

This figure "fig7.gif" is available in "gif" format from:

<http://arxiv.org/ps/astro-ph/9801311v1>

This figure "fig9a.gif" is available in "gif" format from:

<http://arxiv.org/ps/astro-ph/9801311v1>

This figure "fig9b.gif" is available in "gif" format from:

<http://arxiv.org/ps/astro-ph/9801311v1>

This figure "fig9c.gif" is available in "gif" format from:

<http://arxiv.org/ps/astro-ph/9801311v1>

This figure "fig9d.gif" is available in "gif" format from:

<http://arxiv.org/ps/astro-ph/9801311v1>